Research Square

Preprints are preliminary reports that have not undergone peer review.
They should not be considered conclusive, used to inform clinical practice,
or referenced by the media as validated information.

Fixed-Face-Area Closure Reconstruction in Coarse-Grained Loop Quantum Gravity

Shengliang Dong

dshljiayou@gmail.com

Independent Researcher https://orcid.org/0009-0007-0074-6119

Research Article

Keywords: loop quantum gravity, coarse graining, closure constraint, polyhedral geometry

Posted Date: September 1st, 2026

DOI: https://doi.org/10.21203/rs.3.rs-10701057/v1

License: This work is licensed under a Creative Commons Attribution 4.0 International License.
Read Full License

Additional Declarations: The authors declare no competing interests.

Fixed-Face-Area Closure Reconstruction in Coarse-Grained Loop Quantum Gravity

Shengliang Dong
Independent Researcher, Chengdu 610500, China
dshljiayou@gmail.com

Abstract

Coarse graining a spin-network region can leave transported boundary fluxes with a nonzero closure defect. A closed polyhedral comparison geometry then requires a reconstruction prescription, but the usual $SL(2,\mathbb{C})$ closure boost generally changes individual face areas and can spoil area matching with neighbouring regions. We formulate a weighted nearest-closure reconstruction that preserves every face area and leaves the canonical holonomy–flux data unchanged. Near any regular closed N-valent configuration, the reconstruction has a smooth, locally unique, $SO(3)$-equivariant branch; its numerical evaluation reduces to a three-dimensional multiplier equation, independent of N. The small-defect expansion gives an analytic face-resolved response and a quadratic reconstruction cost. In 200 random six-face tests the closure, area, and covariance residuals remain below 7×10^{-16}, and a coupled solver enforces all closure and shared-area-normal constraints on a three-node cycle to the same numerical scale. The construction therefore provides a reproducible fixed-area boundary readout while keeping the canonical fluxes separate. Complete curvature information still requires the internal holonomies and transport data.

Keywords: loop quantum gravity; coarse graining; closure constraint; polyhedral geometry

1 Introduction

On a fixed graph, loop quantum gravity assigns a copy of $T^*SU(2)$ to every oriented edge. When the Gauss constraint closes the area vectors at a node, an N-valent node is dual to a convex N-faced polyhedron whose face areas are the flux norms [1–3]. The source and target fluxes of an edge have equal norm after parallel transport. This area-matching condition glues neighbouring polyhedra into a twisted geometry, even when the full polygonal shapes of the shared face differ [4–7].

The individual norms matter as soon as two coarse-grained regions share a boundary face. Their common spin label fixes one area at both ends of the edge. If closure is restored independently at the two regions by a transformation that changes those norms, the shared face generally acquires two different areas before the stronger shape-matching problem is even considered. Livine's $SL(2,\mathbb{C})$ boost provides exact closure but changes the individual spinor norms and can therefore break boundary matching constraints [8, 9]. The problem addressed here is to construct a closed polyhedral comparison geometry while preserving every prescribed face area.

Our main result can be stated without the six-face specialization. Fix positive areas A_f and weights w_f. Near any closed configuration whose normals are not all collinear, the weighted nearest closed point on the product of fixed-area spheres forms a unique smooth local branch and transforms covariantly under $SO(3)$. Its KKT system reduces to one three-component multiplier equation regardless of the valence N. The reconstruction is a derived geometric representative; it does not replace the canonical boundary fluxes.

This question arises because coarse graining changes the closed-node picture. Gauge fixing the internal graph of a bounded region to an effective vertex leaves self-loops with internal

holonomy data, while the transported boundary fluxes need not close [8, 10, 11]. The defect records the closure component of curvature-dependent boundary data and depends on the maximal tree used for transport. Internal holonomies and transport data contain the complementary information. Loopy, tagged, and bubble networks retain such data in an enlarged coarse-node description [10, 12]; $U(N)$ flows remain within a fixed moment-map sector [8, 13]; and group-valued closure treats curved polyhedra directly [14, 15]. These constructions preserve different data and answer different questions.

For a coarse-grained state with transported flux expectations X_f and spin-fixed areas A_f, the reconstructed normals $\widetilde{n}_f = \pi_w(X)_f/A_f$ define a closed coherent-intertwiner comparison geometry at the same spins [3, 6, 16]. The scalar cost $\mathcal{R}_w^2$ measures the displacement to that geometry, while the shape tensor Q records its directional response. Neither quantity is a complete curvature observable: both diagnose the selected boundary reconstruction, whereas the internal holonomies and transport data remain part of the coarse-grained state.

The six-face case connects the general construction to cubical and hypercuboidal sectors used in loop and spin-foam calculations [17–20]. Inside a nondegenerate realization chamber, the projected vectors determine a deformable convex hexahedron. A coupled projection on adjacent nodes also preserves the oppositely oriented area normal of their shared face after holonomy transport. The same regular-point argument extends to finite graphs, while full polygonal shape matching still requires the intrinsic edge lengths of each shared face.

Section 2 explains why the closed representative belongs to the derived-observable sector. Sections 3–4 construct the map and its small-defect response. Sections 5– 7 treat graph matching, comparison with existing prescriptions, and numerical verification before the final discussion of applicability.

2 Loopy-node closure and the geometric obstruction

Identify $\mathfrak{su}(2)^* \simeq \mathbb{R}^3$ using an invariant inner product. Let X_f, $f = 1, \dots, N$, be the outward fluxes of N external edges, all oriented away from a node. An internal self-loop carries $(g, J) \in T^*SU(2)$. With a left-trivialisation, its contribution to the node moment map is

$$\mu_\circ(g, J) = J - \mathrm{Ad}^*_{g^{-1}} J. \tag{1}$$

The Gauss constraint reads

$$G = \sum_{f=1}^{N} X_f + \mu_\circ = 0. \tag{2}$$

Sign changes caused by alternative orientation conventions do not affect the argument.

If the same N vectors are area normals of a closed convex polyhedron, Minkowski closure requires

$$C(X) := \sum_{f=1}^{N} X_f = 0. \tag{3}$$

Equations (2) and (3) imply $\mu_\circ = 0$, or $J = \mathrm{Ad}^*_{g^{-1}} J$. This does not force g to be the identity; it restricts the loop to the commuting sector. Generic non-collinear loop holonomy–flux data are excluded.

A canonical change of external variables would be an attractive repair. We use the following standard moment-map fact to rule it out within the original constraint system.

Lemma 1 (Equivariant symplectic obstruction)**.** *Let (P, ω, C) be a connected Hamiltonian $SU(2)$-space. If $\Phi : P \to P$ is an $SU(2)$-equivariant symplectomorphism, then $C \circ \Phi = C$ after the conventional normalization of the moment map. In particular, no such map sends a generic nonzero closure defect to zero.*

Proof. Both C and $C \circ \Phi$ are moment maps for the same group action because Φ is symplectic and equivariant. Their difference is therefore a constant in $(\mathfrak{su}(2)^*)^{SU(2)}$ [21]. This invariant subspace is zero for the semisimple group $SU(2)$, so the two moment maps coincide. □

Thus a closed geometric representative may be defined as a derived function of the canonical data. Its realization as a new set of canonical fluxes requires extra variables or a modified reduction; here it is retained as a derived observable.

3 Fixed-face-area nearest-closure reconstruction

Fix an integer $N \geq 3$, positive areas A_f, and weights $w_f > 0$. The fixed-area configuration space is

$$\mathcal{S}_A = \prod_{f=1}^{N} S^2_{A_f}, \qquad S^2_A = \{X \in \mathbb{R}^3 : \|X\| = A\}. \tag{4}$$

Give it the $SO(3)$-invariant product metric

$$\langle u, v \rangle_w = \sum_{f=1}^{N} w_f^{-1} u_f \cdot v_f. \tag{5}$$

The closed subset is $\mathcal{C}_A = F^{-1}(0)$, where $F(X) = \sum_f X_f$.

Remark 2 (Permutation-symmetric baseline)**.** *Within the class of diagonal product metrics in Eq. (5), invariance under all permutations of equally resolved face labels requires all w_f to be equal, up to an irrelevant common scale. We therefore use equal weights as the intrinsic baseline. Nonuniform weights encode face-dependent resolution or uncertainty specified independently of the reconstructed shape.*

Remark 3 (Chordal and intrinsic distances)**.** *Let θ_f be the angle between X_f and Y_f on $S^2_{A_f}$, so that the intrinsic distance is $d_f = A_f \theta_f$. The face contribution to Eq. (7) obeys*

$$\frac{1}{2w_f}\|Y_f - X_f\|^2 = \frac{A_f^2}{w_f}(1 - \cos\theta_f) = \frac{d_f^2}{2w_f} + O\left(\frac{d_f^4}{w_f A_f^2}\right). \tag{6}$$

Thus chordal and intrinsic squared-distance objectives induce the same tangent metric, the same linear correction in Eq. (11), and the same quadratic minimum cost in Eq. (12). Their agreement through these orders is independent of which of the two distances is used. Beyond this order, the objective is part of the reconstruction prescription: different invariant distances can select different nonlinear representatives. The chordal choice has the practical advantage of the three-dimensional multiplier reduction below.

Theorem 4 (Local fixed-area closure)**.** *Let $Y^0 \in \mathcal{C}_A$ be a closed configuration whose face normals are not all collinear. There are neighbourhoods $U \subset \mathcal{S}_A$ of Y^0 and $V \subset \mathcal{C}_A$ of Y^0 such that, for every $X \in U$, the objective*

$$E_X(Y) = \frac{1}{2}\sum_{f=1}^{N} w_f^{-1}\|Y_f - X_f\|^2. \tag{7}$$

has exactly one stationary point $\pi_w(X)$ in V, and this point is a strict local minimizer. The branch depends smoothly on X. It is $SO(3)$-covariant in the sense that rotating the reference configuration, input, and selected branch by the same $R \in SO(3)$ preserves the construction.

Proof. For $u_f \in T_{Y_f^0} S^2_{A_f}$, $dF_{Y^0}(u) = \sum_f u_f$. If a vector $a \in \mathbb{R}^3$ annihilates its image, then $a \cdot u_f = 0$ for every tangent vector u_f; hence a is parallel to every face normal. Non-collinearity gives $a = 0$, so dF is surjective. The regular-value theorem makes $\mathcal{C}_A$ a smooth codimension-three submanifold near Y^0.

The KKT equations on the branch through $(X, Y, \lambda) = (Y^0, Y^0, 0)$ reduce to Eq. (9) below. Write its closure equation as $H(\lambda, X) = 0$. At the reference point,

$$\partial_\lambda H(0, Y^0) = -\sum_{f=1}^{N} w_f (I - n_f^0 n_f^{0\mathsf{T}}) = -M(Y^0). \tag{8}$$

The matrix is invertible because the normals are not all collinear. The implicit function theorem gives a unique smooth multiplier $\lambda(X)$ and a unique stationary point $Y(X)$ in V. At $X = Y^0$, the constrained Hessian of the objective is the positive metric (5); positivity persists after shrinking U and V, so this stationary point is a strict local minimum. Finally, $\mathcal{C}_A$ and the objective are rotation invariant. Applying the same argument at RY^0 and using local uniqueness gives the stated covariance of the family of branches. □

Compactness of $\mathcal{S}_A$ makes the existence statement global: since $\mathcal{C}_A$ is closed, the minimum of E_X on $\mathcal{C}_A$ is attained whenever $\mathcal{C}_A$ is nonempty. The strict generalized polygon inequality $\max_f A_f < \sum_{g \neq f} A_g$ places the fixed-area data in the regime where $\mathcal{C}_A$ contains noncollinear configurations. At each such regular closed configuration, Theorem 4 refines global attainment by furnishing a smooth, locally isolated minimizing branch.

Corollary 5 (Three-dimensional multiplier reduction)**.** *On the local branch of Theorem 4, the $3N$ reconstructed components are determined by a single multiplier $\lambda \in \mathbb{R}^3$ through*

$$\widetilde{X}_f(\lambda) = A_f \frac{X_f - w_f \lambda}{\|X_f - w_f \lambda\|}, \qquad \sum_{f=1}^{N} \widetilde{X}_f(\lambda) = 0. \tag{9}$$

Solving the second equation gives $\pi_w(X) = (\widetilde{X}_f)$.

Proof. The KKT stationarity equation at each face makes the reconstructed vector parallel to $X_f - w_f \lambda$; its fixed norm gives the first relation. The closure constraint gives the second. The implicit-function argument in Theorem 4 supplies the local solution branch. □

Corollary 5 is a three-dimensional coordinate description of the branch connected to Y^0. The chart continues while every denominator is nonzero and the Jacobian $\partial_\lambda H$ remains nonsingular; a vanishing denominator or a loss of rank marks its boundary.

3.1 The six-face realization sector

Theorem 4 applies at every valence. In the $N = 6$ sector, hexahedral combinatorics follows after imposing an additional realization condition: Y^0 lies in the interior of the stratum of a simple, strictly convex six-faced polyhedron: its normals positively span $\mathbb{R}^3$, all six faces have positive area, and no vertex or face incidence is about to degenerate. Minkowski's theorem reconstructs a unique convex polyhedron up to translation. Openness of this nondegenerate realization stratum then retains the hexahedral combinatorial type for sufficiently small perturbations; crossing its boundary may change the type or remove a face [3, 22]. Thus Theorem 4 supplies a local closed-vector representative at arbitrary valence and a deformable hexahedron throughout this six-face realization chamber.

4 Linear response and geometric observables

Let $n_f = X_f/A_f$ and $P_f = I - n_f n_f^{\mathsf{T}}$. Define

$$D = \sum_f X_f = -\mu_\circ, \qquad M(X) = \sum_{f=1}^{N} w_f P_f. \tag{10}$$

For any $a \in \mathbb{R}^3$, $a^{\mathsf{T}} M a = \sum_f w_f \|P_f a\|^2$. Hence M is positive definite precisely when the normals are not all collinear.

Proposition 6 (Small-defect response)**.** *In the neighbourhood of Theorem 4, the correction $\delta_f = \widetilde{X}_f - X_f$ and the minimum reconstruction cost obey*

$$\delta_f = -w_f P_f M^{-1} D + O(\|D\|^2), \tag{11}$$

$$\mathcal{R}_w^2(X) := \frac{1}{2}\sum_f w_f^{-1}\|\delta_f\|^2 = \frac{1}{2} D^{\mathsf{T}} M^{-1} D + O(\|D\|^3). \tag{12}$$

Proof. Expand Eq. (9) around $\lambda = 0$. Normalization to the fixed-area sphere gives $\delta_f = -w_f P_f \lambda + O(\|\lambda\|^2)$. Closure implies $D - M\lambda + O(\|\lambda\|^2) = 0$, so $\lambda = M^{-1} D + O(\|D\|^2)$. Substitution proves (11); inserting it into the quadratic cost yields (12). □

The scalar $\mathcal{R}_w^2$ measures how far the transported fixed-area boundary data lie from the closed fixed-area sector. A complementary shape tensor of the reconstructed geometry is

$$Q(X) = \sum_{f=1}^{N} A_f \widetilde{n}_f \widetilde{n}_f^{\mathsf{T}}, \qquad \widetilde{n}_f = \widetilde{X}_f / A_f. \tag{13}$$

Under a gauge rotation, $Q \mapsto RQR^{\mathsf{T}}$; consequently $\operatorname{tr} Q^2$ and $\det Q$ are gauge invariant. In a coarse-graining calculation, $\mathcal{R}_w^2$ can be used to compare how strongly different regions or resolution choices displace the transported data from the fixed-area closure sector. The invariants of Q distinguish directional shape responses that have the same defect norm. For a fixed-spin coherent-intertwiner comparison, they quantify the scalar displacement and anisotropy of the selected closed peak geometry. They are reconstruction diagnostics, not order parameters for the full bulk curvature; internal holonomies and transport data retain the information not contained in D.

Corollary 7 (Orthogonal six-face baseline)**.** *For equal weights $w_f = 1$ and a closed reference configuration with normals $\{\pm e_1, \pm e_2, \pm e_3\}$, one has $M = 4I$. Consequently,*

$$\delta_f = -\frac{1}{4} P_f D + O(\|D\|^2), \qquad \mathcal{R}^2(X) = \frac{1}{8}\|D\|^2 + O(\|D\|^3). \tag{14}$$

Proof. Each pair of opposite normals contributes $2(I - e_a e_a^{\mathsf{T}})$; summing over $a = 1, 2, 3$ gives $M = 4I$. Proposition 6 then gives Eq. (14). □

5 Coupled reconstruction on adjacent cells and finite graphs

A nodewise map is insufficient on a graph because it can rotate the two fluxes of a shared edge differently. Consider adjacent six-valent nodes A and B. Let $h_{BA} \in SU(2)$ denote parallel transport from the frame of B to that of A, and let s_A and s_B label the common face, with equal fixed area. Before identifying frames, the geometric flux-matching condition is

$$Y^A_{s_A} + \mathrm{Ad}_{h_{BA}}\, Y^B_{s_B} = 0. \tag{15}$$

This is the standard oriented area-normal relation carried by an LQG edge [23]. Define transported variables $\bar{X}_f^B = \mathrm{Ad}_{h_{BA}} X_f^B$ and $\bar{Y}_f^B = \mathrm{Ad}_{h_{BA}} Y_f^B$. Since the adjoint action is an isometry, it preserves all areas and the weighted cost. In the common frame, and dropping the bar from the transported B variables, Eq. (15) becomes

$$Y_{s_A}^A + Y_{s_B}^B = 0. \tag{16}$$

Define $\mathcal{C}_{AB}$ by Eq. (16) together with $\sum_f Y_f^A = \sum_f Y_f^B = 0$, and minimize the sum of the two node costs

$$E_{AB} = \frac{1}{2} \sum_{i=A,B} \sum_{f=1}^{6} (w_f^i)^{-1} \|Y_f^i - X_f^i\|^2. \tag{17}$$

Proposition 8 (Local matched reconstruction)**.** *Let $Y^0 \in \mathcal{C}_{AB}$ be a matched pair at which the differential of the two closure constraints and the two independent tangential components of Eq. (16) has full rank. Then all input pairs sufficiently close to Y^0 possess a unique local minimizer of Eq. (17) on $\mathcal{C}_{AB}$. The minimizer is smooth and covariant under a simultaneous frame rotation.*

Proof. Equal fixed norms make the radial component of Eq. (16) dependent, so the stated full-rank condition makes $\mathcal{C}_{AB}$ a smooth local submanifold. The objective Hessian at coincident input and output is the positive product metric. The implicit-function argument of Theorem 4, now applied to the regular coupled constraints, gives a unique smooth local minimum. Simultaneous rotational covariance follows from invariance and uniqueness. □

The full-rank hypothesis is nonempty and includes the orthogonal hexahedral baseline. Take the two sets of normals to be $\{\pm e_1, \pm e_2, \pm e_3\}$, with shared normals e_1 at A and $-e_1$ at B. Suppose multipliers $a, b \in \mathbb{R}^3$ for the two closure differentials and $c \in e_1^\perp$ for the two independent shared-face components annihilate every tangent variation. Variations of the five nonshared faces at A require a to be parallel to $-e_1$, e_2, and e_3, hence $a = 0$; the same argument gives $b = 0$. Independent tangential variations of the shared pair then give $c = 0$. The annihilator is therefore trivial, proving the required rank at this reference pair and, by openness, throughout a neighbourhood of it.

For computation, eliminate $Y_{s_B}^B$ by writing the shared pair as S and $-S$. For closure multipliers λ_A, λ_B, the other faces retain the form of Eq. (9). The stationarity condition for the two shared-face cost terms makes S parallel to their weighted difference, giving

$$S = A_s \frac{X_{s_A}^A / w_{s_A}^A - X_{s_B}^B / w_{s_B}^B - \lambda_A + \lambda_B}{\left\| X_{s_A}^A / w_{s_A}^A - X_{s_B}^B / w_{s_B}^B - \lambda_A + \lambda_B \right\|}. \tag{18}$$

The two closure equations form a six-dimensional root problem.

Corollary 9 (Finite-graph extension)**.** *Let a finite graph carry fixed-area vector sets at its nodes and one oppositely oriented area-normal constraint for each shared face. At any matched closed configuration where the differential of all closure and independent matching constraints has full rank, the sum of the nodewise costs has a unique smooth local minimizer in a neighbourhood of that configuration.*

Proof. The regular-value and positive-Hessian argument of Proposition 8 applies to the product of all node configuration spaces. □

The computational reduction also extends edge by edge: Eq. (18) is used for every shared pair, and the closure equations supply $3|V|$ equations for the $3|V|$ node multipliers. On graphs with cycles these equations are solved simultaneously. Equation (15) matches the transported oriented area normal supplied by one LQG edge. Matching all intrinsic edge lengths of the polygonal face adds the stronger shape-matching condition that separates generic twisted geometries from Regge geometries [1, 2, 4, 5].

6 Relation to existing boundary prescriptions

The prescriptions in Table 1 implement distinct choices of which coarse-grained data are retained and which geometric representative is constructed. The final row is the fixed-face-area selection studied here.

Table 1: Related treatments of closure and boundary geometry, with the data preserved by each prescription.

Prescription	Defect	Preserved area data	Output or role
Loopy or tagged node	retained	original boundary labels	enlarged coarse-node data
$U(N)$ deformation	retained	total area	deformation within a fixed moment-map sector
$SL(2,\mathbb{C})$ boost	removed	holomorphic F_{ij}; face areas change	closed spinors with rest area
Group-valued closure	encoded non-Abelianly	curved face holonomies	curved-polyhedron phase space
Fixed-face-area projection	removed from derived output	every individual A_f	nearest closed vector geometry

The first choice keeps the canonical coarse-grained information and is appropriate when the defect itself is part of the effective state [10]. The $U(N)$ generators are $SU(2)$-invariant spinor bilinears; their flows preserve the global moment map and total area, so they deform rather than close a generic nonclosed configuration [8, 13]. The $SL(2,\mathbb{C})$ boost instead reaches the closure surface, but the transformed total area is the rest area and every individual spinor norm is generally changed. Livine noted that this can break the matching constraints on the boundary edges [8, 9]. Fixed individual areas therefore prevent this particular network-level mismatch and define a distinct reconstruction problem.

The group-valued row addresses the neighbouring reconstruction problem in which curvature replaces additive Euclidean closure by a group product or Bianchi identity [14, 15, 24]. Here the canonical coarse-grained fluxes and their loop holonomies are left untouched; the reconstruction acts on their associated Euclidean polyhedral readout. Mathematical local uniqueness holds after the areas, weights, and objective have been fixed. These data define a reproducible geometric selection rule through π_w; different invariant metrics encode different face resolutions and select correspondingly different representatives.

7 Numerical verification

We solve the multiplier equation in Corollary 5 with a three-dimensional Newton-type root finder. The reference configuration is a noncubic rectangular box with opposite face-vector magnitudes $(1.20, 0.95, 1.10)$; all six normals are then perturbed by unequal rotations without changing their norms. The representative, random-ensemble, and adjacent-cell results below use the permutation-symmetric choice $w_f = 1$. Separately labelled nonuniform weights test the general weighted formulas and their implementation. The script and machine-readable results accompany this article.

Calculations use double precision, a root-residual acceptance threshold of 5×10^{-10}, and the fixed random seed 20260814. On the regular stationary branch, the fth tangent block of the constrained Lagrangian Hessian is

$$\frac{\|X_f - w_f\lambda\|}{A_f w_f} I\big|_{T_{\tilde{X}_f} S^2_{A_f}}. \tag{19}$$

Consequently, the minimum of these six coefficients is a conservative lower bound after restriction to the closure tangent space. Positivity of this quantity is the Hessian check quoted below.

For a representative input with $\|D\| = 0.29304$, the solver checks give a closure residual of 2.4×10^{-16} and a maximum individual-area residual of 2.2×10^{-16}. An independent common rotation changes the equivariance test by 3.3×10^{-16}. The normalized shape invariants

$$I_2 = \frac{3 \operatorname{tr} Q^2}{(\operatorname{tr} Q)^2}, \qquad I_3 = \frac{27 \det Q}{(\operatorname{tr} Q)^3} \tag{20}$$

evaluated with the same second-moment formula change from $(I_2, I_3) = (1.012678, 0.981268)$ on the transported normals to $(1.012654, 0.981298)$ in the closed representative, while $\operatorname{tr} Q = \sum_f A_f = 6.5$ remains fixed. Figure 1 shows the transported and closed vectors. The black arrow in the left panel is the defect D; the right panel reports the numerically vanishing sum of the reconstructed vectors.

We additionally generated 200 random fixed-area perturbations with amplitudes up to 0.22 radians and applied an independent random rotation to every case. For each solution we evaluated the regular-branch KKT Hessian. The full ensemble retained a minimum Hessian lower bound of 0.888. The largest closure, area, and covariance residuals were respectively 6.2×10^{-16}, 2.2×10^{-16}, and 6.7×10^{-16}. The first two are solver checks; covariance and Hessian positivity test the equivariant regular branch away from the representative opposite-face pattern. The equal-weight ensemble defines the baseline geometry. As a separate implementation stress test, we repeat 100 of these inputs with fixed nonuniform positive weights. Its largest closure, area, and covariance residuals are 7.2×10^{-16}, 4.4×10^{-16}, and 8.9×10^{-16}, while its minimum Hessian lower bound is 0.751.

For the adjacent-cell test, both cells and their shared pair are perturbed independently. The input shared-face mismatch is 0.11629, and separate nodewise projections leave a mismatch of 0.11604. The coupled reconstruction of Sec. 5 reduces both cell-closure residuals and the shared-face residual below 1.5×10^{-17}, while the maximum area error is 2.2×10^{-16} and the simultaneous-rotation covariance residual is 4.4×10^{-16}.

We next use three six-valent nodes in a cycle, with identity edge transports in a common gauge and three independently perturbed shared pairs. The largest input mismatch is 0.11417; separate nodewise projections leave 0.07428. The joint 9-variable root problem gives maximum node-closure, shared-face, area, and covariance residuals below 5.1×10^{-16}. This realizes the simultaneous cycle constraints in Corollary 9 for one regular graph configuration.

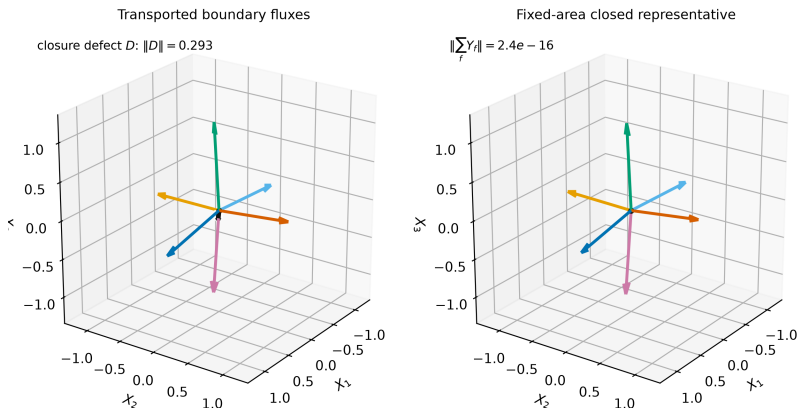


Figure 1: Six fixed-area vectors before and after nearest-closure reconstruction. In the left panel the black arrow is the closure defect $D = \sum_f X_f$; the reconstructed sum in the right panel is below numerical resolution. Individual norms are unchanged.

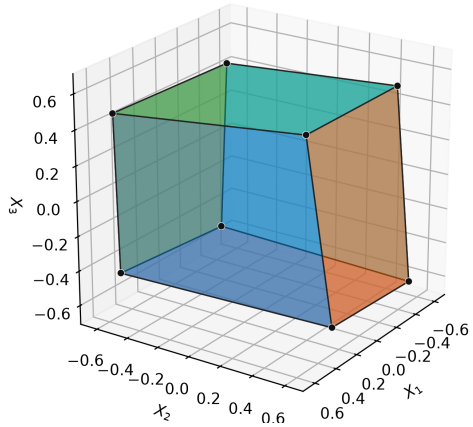


Figure 2: Convex six-face realization of the reconstructed area vectors in the sample case. Black markers show the reconstructed vertices. The six face areas agree with the prescribed norms to a relative error below 6.1×10^{-16}, and the result lies in the local hexahedral realization chamber.

To test the general weighted form of Eq. (12), we scan 26 perturbation amplitudes using the fixed positive weights $(1.00, 1.10, 0.90, 1.20, 1.05, 0.95)$. Define $\delta_f^{\mathrm{lin}} = -w_f P_f M^{-1} D$. The weighted face-resolved error $[\sum_f w_f^{-1} \|\delta_f - \delta_f^{\mathrm{lin}}\|^2]^{1/2}$ scales as $\|D\|^{1.99998}$, directly verifying the remainder in Eq. (11); its relative error scales as $\|D\|^{0.99999}$. The relative difference between the nonlinear minimum and Eq. (12) scales as $\|D\|^{1.0002}$, consistent with the cubic absolute remainder. Figure 3 displays both tests.

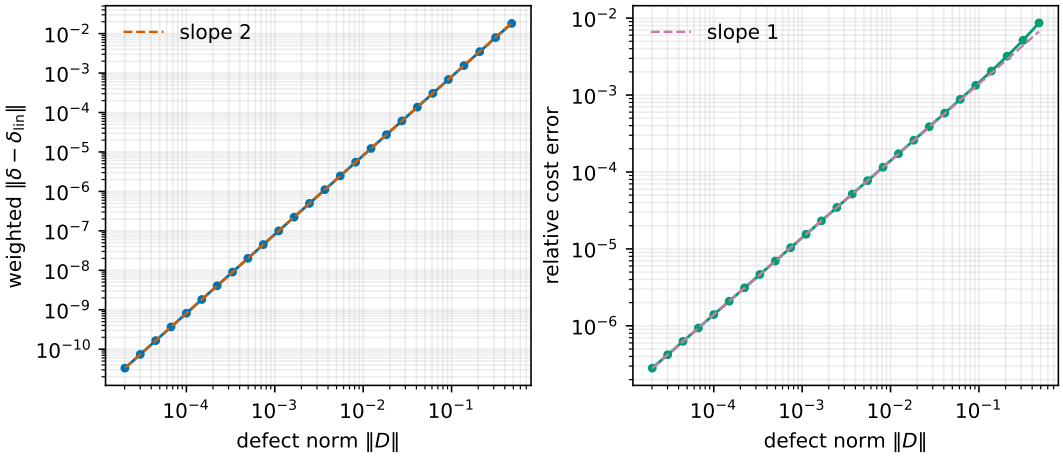


Figure 3: Small-defect response. Left: weighted error of the face-resolved linear prediction, with a slope-two reference. Right: relative error of the quadratic reconstruction cost, with a slope-one reference.

To probe the regularity boundary, take three opposite pairs generated by $n_1 = e_3$, $n_2 = (\sin\eta, 0, \cos\eta)$, and $n_3 = (0, \sin\eta, \cos\eta)$, with the same six areas as above. The normals become collinear as $\eta \to 0$. Over $0.01 \le \eta \le 1.2$, the scan gives $\lambda_{\min}(M) \propto \eta^{1.9995}$ and $\kappa(M) \propto \eta^{-1.9998}$; the largest sampled condition number is 2.25×10^4. For auxiliary perturbations of amplitude 10^{-4}, the minimum denominator in Eq. (9) remains 0.9457 and the Hessian lower bound remains above 0.9954. The scan therefore isolates the loss of rank in M while the other regular-branch conditions remain inactive.

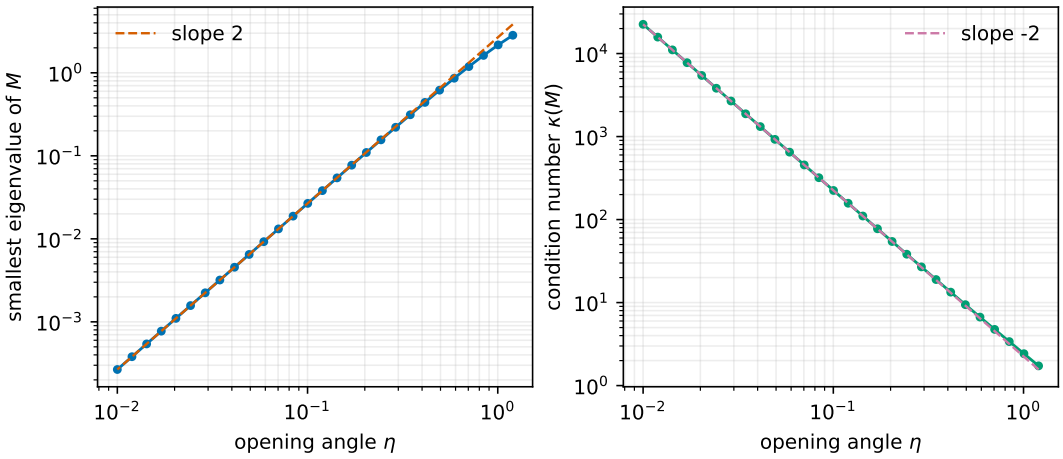


Figure 4: Approach to the collinear regularity boundary. The smallest eigenvalue of M vanishes quadratically (left), while its condition number diverges with inverse quadratic scaling (right).

8 Regime of applicability and extensions

The canonical transported fluxes and the closed geometric representative play distinct roles. The former enter the Gauss law and retain the closure defect generated by coarse graining; the latter describe a closed, fixed-area polyhedron. Lemma 1 shows why the latter is a derived observable: realizing it as a new canonical flux set with the same $SU(2)$ action would require additional phase-space variables or a modified reduction. The reconstructed normals supply a closed peak geometry for a fixed-spin coherent-intertwiner comparison, while $\mathcal{R}_w^2$ and the invariants in Eq. (20) measure its displacement and anisotropy relative to the transported boundary data.

The regular branch continues while the denominators in Eq. (9) remain nonzero and the response matrix M remains nonsingular. In the six-face sector, the branch also remains inside the chosen realization chamber. Vanishing denominators, loss of rank, and realization walls are therefore the three boundaries at which the stationary branch or the polyhedral combinatorics must be reanalysed. The conditioning scan in Fig. 4 resolves the rank-loss boundary independently of the other two conditions.

The curvature-sensitive data retained by this coarse-graining include the internal holonomies together with the transported boundary fluxes. The defect D isolates their closure component, while $\mathcal{R}_w^2$ and Q summarize its scalar reconstruction cost and directional geometric response. The maximal tree used to transport the boundary data fixes the coarse-graining scheme [8]; changing it can therefore change these readouts even though each is invariant under a common local $SU(2)$ rotation.

Corollary 9 extends the local construction to regular finite graphs, with one transported area-normal condition for every shared edge. The three-node test shows that the coupled multiplier equations can satisfy a complete cycle simultaneously. Nontrivial cycle holonomies and Regge gluing add, respectively, transport consistency and the intrinsic edge-length conditions of polygonal shape matching. A dynamical formulation requires either a symplectic lift of the reconstruction or insertion of its derived observables into a separately specified constraint and evolution scheme. Nonuniform weights enter that formulation as prescribed face-resolution data. Controlled graphs for elementary loop-gravity blocks provide a setting for this extension [25].

Deformability has a limited but useful role. Within a rigid cuboid, fixed face areas leave no shape response, whereas the six-face sector has tangent directions that absorb a small closure defect into changed normals while preserving the boundary areas. The shape change reads out this component; full curvature still requires loop holonomies and transport data.

9 Conclusion

We constructed a fixed-face-area nearest-closure map for coarse-grained LQG boundaries. For arbitrary valence, the map has a smooth, locally unique, rotation-equivariant branch near every regular closed configuration, and Corollary 5 reduces its evaluation to a three-dimensional root problem. The small-defect expansion gives the face-resolved response and the quadratic reconstruction cost. Inside a nondegenerate six-face realization chamber the output is a deformable hexahedron, and the coupled finite-graph construction preserves holonomy-transported area normals on shared faces. The numerical tests verify the analytic scaling and enforce the complete set of closure and matching constraints on a three-node cycle. The map therefore supplies a reproducible closed comparison geometry without changing the canonical fluxes or creating an area mismatch between adjacent regions. Nontrivial cycle holonomies, polygonal shape matching on larger graphs, and a dynamical or quantum realization of the response observables remain open.

Data and code availability

The reconstruction script, numerical outputs, and figure-generation procedure are included with the source files of this manuscript. No observational or experimental data were used.

Conflict of interest

The author declares no conflict of interest.

Use of language-model-assisted tools

Language-model-assisted tools were used during manuscript organization and language editing. The author remains responsible for the mathematical arguments, numerical calculations, references, and conclusions.

References

[1] Laurent Freidel and Simone Speziale. Twisted geometries: A geometric parametrisation of SU(2) phase space. *Phys. Rev. D*, 82:084040, 2010. doi: 10.1103/PhysRevD.82.084040.

[2] Carlo Rovelli and Simone Speziale. On the geometry of loop quantum gravity on a graph. *Phys. Rev. D*, 82:044018, 2010. doi: 10.1103/PhysRevD.82.044018.

[3] Eugenio Bianchi, Pietro Donà, and Simone Speziale. Polyhedra in loop quantum gravity. *Phys. Rev. D*, 83:044035, 2011. doi: 10.1103/PhysRevD.83.044035.

[4] Bianca Dittrich and James P. Ryan. Simplicity in simplicial phase space. *Phys. Rev. D*, 82: 064026, 2010. doi: 10.1103/PhysRevD.82.064026.

[5] Bekir Baytaş, Eugenio Bianchi, and Nelson Yokomizo. Gluing polyhedra with entanglement in loop quantum gravity. *Phys. Rev. D*, 98:026001, 2018. doi: 10.1103/PhysRevD.98.026001.

[6] Andrea Calcinari, Laurent Freidel, Etera R. Livine, and Simone Speziale. Twisted geometries coherent states for loop quantum gravity. *Class. Quantum Grav.*, 38:025004, 2021. doi: 10.1088/1361-6382/abc273.

[7] Bianca Dittrich and José Padua-Argüelles. Twisted geometries are area-metric geometries. *Phys. Rev. D*, 109:026002, 2024. doi: 10.1103/PhysRevD.109.026002.

[8] Etera R. Livine. Deformation operators of spin networks and coarse-graining. *Class. Quantum Grav.*, 31:075004, 2014. doi: 10.1088/0264-9381/31/7/075004.

[9] Etera R. Livine. Area propagator and boosted spin networks in loop quantum gravity. *Class. Quantum Grav.*, 36:185009, 2019. doi: 10.1088/1361-6382/ab3d6b.

[10] Christoph Charles and Etera R. Livine. The fock space of loopy spin networks for quantum gravity. *Gen. Relativ. Gravit.*, 48:113, 2016. doi: 10.1007/s10714-016-2107-5.

[11] Alexandre Feller and Etera R. Livine. Quantum surface and intertwiner dynamics in loop quantum gravity. *Phys. Rev. D*, 95:124038, 2017. doi: 10.1103/PhysRevD.95.124038.

[12] Laurent Freidel and Etera R. Livine. Bubble networks: Framed discrete geometry for quantum gravity. *Gen. Relativ. Gravit.*, 51:9, 2019. doi: 10.1007/s10714-018-2493-y.

[13] Laurent Freidel and Etera R. Livine. The fine structure of SU(2) intertwiners from U(N) representations. *J. Math. Phys.*, 51:082502, 2010. doi: 10.1063/1.3473786.

[14] Hal M. Haggard, Muxin Han, and Aldo Riello. Encoding curved tetrahedra in face holonomies: Phase space of shapes from group-valued moment maps. *Ann. Henri Poincare*, 17:2001–2048, 2016. doi: 10.1007/s00023-015-0455-4.

[15] Christoph Charles and Etera R. Livine. The closure constraint for the hyperbolic tetrahedron as a Bianchi identity. *Gen. Relativ. Gravit.*, 49:92, 2017. doi: 10.1007/s10714-017-2255-2.

[16] Etera R. Livine and Simone Speziale. A new spinfoam vertex for quantum gravity. *Phys. Rev. D*, 76:084028, 2007. doi: 10.1103/PhysRevD.76.084028.

[17] Aristide Baratin, Cecilia Flori, and Thomas Thiemann. The holst spin foam model via cubulations. *New J. Phys.*, 14:103054, 2012. doi: 10.1088/1367-2630/14/10/103054.

[18] Benjamin Bahr and Sebastian Steinhaus. Investigation of the spinfoam path integral with quantum cuboid intertwiners. *Phys. Rev. D*, 93:104029, 2016. doi: 10.1103/PhysRevD.93.104029.

[19] Benjamin Bahr and Sebastian Steinhaus. Hypercuboidal renormalization in spin foam quantum gravity. *Phys. Rev. D*, 95:126006, 2017. doi: 10.1103/PhysRevD.95.126006.

[20] Courtney Allen, Florian Girelli, and Sebastian Steinhaus. Numerical evaluation of spin foam amplitudes beyond simplices. *Phys. Rev. D*, 105:066003, 2022. doi: 10.1103/PhysRevD.105.066003.

[21] Ana Cannas da Silva. *Lectures on Symplectic Geometry.* Springer, Berlin, 2001. doi: 10.1007/978-3-540-45330-7.

[22] Rolf Schneider. *Convex Bodies: The Brunn–Minkowski Theory.* Cambridge University Press, Cambridge, 2 edition, 2014. doi: 10.1017/CBO9781139003858.

[23] Laurent Freidel, Marc Geiller, and Jonathan Ziprick. Continuous formulation of the loop quantum gravity phase space. *Class. Quantum Grav.*, 30:085013, 2013. doi: 10.1088/0264-9381/30/8/085013.

[24] Laurent Freidel and Jonathan Ziprick. Spinning geometry = twisted geometry. *Class. Quantum Grav.*, 31:045007, 2014. doi: 10.1088/0264-9381/31/4/045007.

[25] Mehdi Assanioussi and Etera R. Livine. Elementary blocks of loop quantum gravity. *Class. Quantum Grav.*, 43:155024, 2026. doi: 10.1088/1361-6382/ae910e.

Supplementary Files

This is a list of supplementary files associated with this preprint. Click to download.

- GRGreproducibilitymaterialv3.zip